

MULTIRESOLUTION LOCAL SMOOTHNESS DETECTION IN NON-UNIFORMLY SAMPLED MULTIVARIATE SIGNALS

SARA AVESANI, GIANLUCA GIACCHI, AND MICHAEL MULTERER

ABSTRACT. Inspired by edge detection based on the decay behavior of wavelet coefficients, we introduce a (near) linear-time algorithm for detecting the local regularity in non-uniformly sampled multivariate signals. Our approach quantifies regularity within the framework of microlocal spaces introduced by Jaffard. The central tool in our analysis is the fast samplelet transform, a distributional wavelet transform tailored to scattered data. We establish a connection between the decay of samplelet coefficients and the pointwise regularity of multivariate signals. As a by product, we derive decay estimates for functions belonging to classical Hölder spaces and Sobolev-Slobodeckij spaces. While traditional wavelets are effective for regularity detection in low-dimensional structured data, samplelets demonstrate robust performance even for higher dimensional and scattered data. To illustrate our theoretical findings, we present extensive numerical studies detecting local regularity of one-, two- and three-dimensional signals, ranging from non-uniformly sampled time series over image segmentation to edge detection in point clouds.

1. INTRODUCTION

A typical trait of real-world signals is their varying local regularity, as they feature both smooth regions and abrupt discontinuities, or singularities. In visual data analysis, these discontinuities correspond to *edges*, which are boundaries that separate distinct regions or objects. The task of identifying such edges, known in computer graphics as *edge detection*, has been a central challenge in computer vision for decades, leading to the development of numerous methods for detecting discontinuities, see [18, 28, 30] for an overview. Differently from earlier works, our goal is not only to detect discontinuities in non-uniformly sampled signals, but also singularities in their derivatives. For this purpose, we develop an algorithm for efficiently detecting local smoothness in multivariate signals, leveraging a discrete multiresolution analysis technique tailored for scattered data, the so-called *samplelet transform*, see [11].

Multiresolution analysis has emerged as a powerful tool for edge detection, developing a mathematical framework for decomposing signals and images into multiple levels of detail. Its most widely used tool, the *(fast) wavelet transform*, is known for its ability to capture both spatial and frequency information simultaneously, see [17, 22], and has been extensively applied to edge detection, as in [10, 21, 27, 33]. A key principle underlying wavelet analysis is that the smoothness of a function directly relates to how quickly its wavelet coefficients decay: smooth regions exhibit rapid coefficient decay across scales, while non-smooth regions are characterized by slowly decaying coefficients. A pioneering work in local smoothness detection is [23], where singularities of one-dimensional signals are observed to correspond exactly to the local maxima of its (continuous) wavelet transform across scales. By analyzing the rate of decay of the wavelet coefficients along these maxima, the authors measured the local Hölder exponents. Even though tailored to the analysis of structured data and primarily developed for univariate signals or images, this method has been very influential in local singularity detection.

For smoothness detection in possibly multivariate, non-uniformly sampled signals and, more generally, scattered data, various kernel-based methods have been developed so far, cf. [5, 19, 20, 24, 34]. These methods use kernel functions, often radial basis functions, to measure the similarity or influence between data points. Specifically, kernel-based filters have become popular in image processing for tasks such as smoothing and sharpening, achieved by convolving the image with a predefined kernel. While these methods offer powerful capabilities, their performance is impacted by the ill-conditioning of kernel matrices and the sensitivity to the choice of kernel length-scale parameters. In recent years, neural network approaches have been developed for kernel-based edge detection methods in the framework of scattered data, see, for example, [4, 8, 9, 14, 25, 26, 31, 32] and the references therein. These methods demonstrate the strength of data-driven approaches, though they typically rely on large training datasets, cf. [7].

In this work, we develop a data-driven deterministic multiresolution approach designed not only to detect singularities, but also to classify their type. To overcome the limitation of wavelets requiring structured low-dimensional data, we employ *samplets*, which are discrete, localized signed measures specifically constructed on the underlying scattered data. They can be considered as *distributional wavelets*, meaning that mother wavelets are allowed to be linear combinations of Dirac- δ -distributions. Samplets find applications in compressed sensing, see [3], deepfake detection, see [13] and kernel learning, see [1, 12]. For our pointwise smoothness analysis, we consider the microlocal spaces defined by Jaffard, see [15], where the author also relates the decay of wavelet coefficients to local regularity of signals. We extend this approach, to the non-uniform regime and present similar bounds for samplelet coefficients, providing a method for detecting local regularity directly from scattered data, without any further structural assumption. To this end, considering the given signal as a discrete signed measure, we employ a change of basis from the basis of Dirac- δ -distributions to the samplelet basis. This change of basis can be performed in linear time using the fast samplelet transform. The suggested approach particularly avoids the long training process needed for neural networks and the difficulties in the construction of wavelets on general data sets. We benchmark our method on one-, two- and three-dimensional signals. The reported run-times match the theoretical (near) linear rate in terms of number of data sites.

The rest of this article is structured as follows. We reserve Section 2 for the preliminaries, i.e., the definition of Jaffard's microlocal spaces, the construction of samplets and the samplelet transform. We relate the decay of samplelet coefficients to microlocal spaces, Hölder classes and Sobolev-Slobodetskij spaces in Section 3. In Section 4 we develop our algorithm for smoothness class detection, and benchmark it in Section 5 on concrete examples. Concluding remarks are stated in Section 6.

Throughout this article, to avoid the repeated use of unspecified generic constants, we write $A \lesssim B$ if A is bounded by a uniform constant times B , where the constant does not depend on any parameters which A and B might depend on. Whereas we write $A \sim B$ if $A \lesssim B$ and $B \lesssim A$.

2. PRELIMINARIES AND NOTATION

This section is structured into three parts. We begin by recalling the idea of microlocal spaces and list some results that will be employed later on. Afterwards, we give a brief overview on the construction of samplets, while the last part is concerned with the fast samplelet transform.

2.1. Pointwise smoothness classes. Let $\Omega \subset \mathbb{R}^d$ denote a region. To measure the local smoothness of a given function, we apply the concept of microlocal spaces from [15]. For a given function $f: \Omega \rightarrow \mathbb{R}$ and a point $\mathbf{x}_0 \in \Omega$, we say that f is in the microlocal space $C^\alpha(\mathbf{x}_0)$, for $\alpha \geq 0$, if there exists a polynomial P of degree $\lfloor \alpha \rfloor$, and a constant $R > 0$, such that for all $\mathbf{x} \in B_R(\mathbf{x}_0) := \{\mathbf{x} \in \mathbb{R}^d : \|\mathbf{x} - \mathbf{x}_0\|_2 \leq R\}$ there holds

$$(1) \quad |f(\mathbf{x}) - P(\mathbf{x} - \mathbf{x}_0)| \lesssim \|\mathbf{x} - \mathbf{x}_0\|_2^\alpha.$$

Observe that, in view of this definition, $C^0(\mathbf{x}_0)$ corresponds to the space of functions that are bounded in a neighborhood of \mathbf{x}_0 .

To provide some context on this notion of smoothness, we recall the definition of the usual (k, ϑ) -Hölder spaces.

Definition 2.1. Let $\Omega \subseteq \mathbb{R}^d$ be closed, $k \in \mathbb{N}$ and $0 < \vartheta \leq 1$. We write $f \in \mathcal{C}^{k, \vartheta}(\Omega)$ if f is k times differentiable in Ω and there holds

$$(2) \quad |\partial^\beta f(\mathbf{x}) - \partial^\beta f(\mathbf{y})| \lesssim \|\mathbf{x} - \mathbf{y}\|_2^\vartheta,$$

for every $|\beta| = k$ and \mathbf{x}, \mathbf{y} in Ω .

Remark 2.2. There always holds $\mathcal{C}^{k, \vartheta}(B_R(\mathbf{x}_0)) \subseteq C^{k+\vartheta}(\mathbf{x}_0)$ with $R > 0$ from (1). However, the reverse inclusion fails, for the regularity of functions in $\mathcal{C}^{k, \vartheta}(B_R(\mathbf{x}_0))$ is much stronger than the pointwise regularity of those in $C^{k+\vartheta}(\mathbf{x}_0)$. For instance, the function $f(x) = x\mathbb{1}_{\mathbb{Q}}(x)$, where $\mathbb{1}_{\mathbb{Q}}$ is the indicator function on rationals, is only continuous in $x = 0$, and from

$$(3) \quad |x\mathbb{1}_{\mathbb{Q}}(x) - x| = |x\mathbb{1}_{\mathbb{R} \setminus \mathbb{Q}}(x)| \leq |x|, \quad x \in \mathbb{R},$$

we infer that it belongs to $C^1(0)$ with arbitrarily large R in (1). However, it is trivial that it cannot belong to $\mathcal{C}^{0,1}(B_R(0))$ for any $R > 0$.

For the benefit of the reader, we report a proof of the inclusion in Remark 2.2.

Proof. The case $k = 0$ is trivial. We may therefore assume $k > 0$, and consider the Taylor expansion of f with integral remainder:

$$\begin{aligned} f(\mathbf{x}) &= \sum_{|\beta| \leq k-1} \frac{\partial^\beta f(\mathbf{x}_0)}{\beta!} (\mathbf{x} - \mathbf{x}_0)^\beta \\ &\quad + \sum_{|\beta|=k} \frac{(\mathbf{x} - \mathbf{x}_0)^\beta}{\beta!} k \int_0^1 (1-t)^{k-1} \partial^\beta f(\mathbf{x}_0 + t(\mathbf{x} - \mathbf{x}_0)) dt \end{aligned}$$

holding for every $\mathbf{x} \in B_R(\mathbf{x}_0)$. We make the ansatz

$$P_k(\mathbf{x} - \mathbf{x}_0) = \sum_{|\beta| \leq k-1} \frac{\partial^\beta f(\mathbf{x}_0)}{\beta!} (\mathbf{x} - \mathbf{x}_0)^\beta + \sum_{|\beta|=k} \frac{\partial^\beta f(\mathbf{x}_0)}{\beta!} (\mathbf{x} - \mathbf{x}_0)^\beta.$$

Then, there holds

$$f(\mathbf{x}) = P_k(\mathbf{x} - \mathbf{x}_0) + r(\mathbf{x})$$

with

$$r(\mathbf{x}) := \sum_{|\beta|=k} \frac{(\mathbf{x} - \mathbf{x}_0)^\beta}{\beta!} k \int_0^1 (1-t)^{k-1} [\partial^\beta f(\mathbf{x}_0 + t(\mathbf{x} - \mathbf{x}_0)) - \partial^\beta f(\mathbf{x}_0)] dt,$$

due to $\int_0^1 (1-t)^{k-1} dt = 1/k$. Now letting $\|\mathbf{x} - \mathbf{x}_0\|_2 \leq R$, there holds for $|\beta| \leq k$ that

$$|\partial^\beta f(\mathbf{x}_0 + t(\mathbf{x} - \mathbf{x}_0)) - \partial^\beta f(\mathbf{x}_0)| \lesssim \|\mathbf{x} - \mathbf{x}_0\|_2^\vartheta$$

and, hence,

$$\begin{aligned} |r(\mathbf{x})| &\leq \sum_{|\beta|=k} |\mathbf{x} - \mathbf{x}_0|^k \frac{k}{\beta!} \int_0^1 (1-t)^k |\partial^\beta f(\mathbf{x}_0 + t(\mathbf{x} - \mathbf{x}_0)) \partial^\beta f(\mathbf{x}_0)| dt \\ &\lesssim \frac{d^k}{k!} \|\mathbf{x} - \mathbf{x}_0\|_2^{k+\vartheta}, \end{aligned}$$

for every $\mathbf{x} \in B_R(\mathbf{x}_0)$, where we used the multinomial theorem in the last step. \square

In view of Remark 2.2, microlocal spaces generalize and localize the concept of Hölder spaces. Therefore, we will refer to the supremum of such α , for which the condition (1) holds true, as the local Hölder exponent of f at \mathbf{x}_0 . The latter quantifies the local smoothness of f at \mathbf{x}_0 .

Remark 2.3. *The definition of microlocal spaces is compatible with functions that are infinitely many times differentiable in a point \mathbf{x}_0 in the following sense. Let $f: \Omega \rightarrow \mathbb{R}$ be infinitely many times differentiable in $\mathbf{x}_0 \in \Omega$. By Taylor expanding f around \mathbf{x}_0 , we have for every $k \in \mathbb{N}$ that*

$$f(\mathbf{x}) = P_k(\mathbf{x} - \mathbf{x}_0) + \sum_{|\beta|=k} r_\beta^{(k)}(\mathbf{x})(\mathbf{x} - \mathbf{x}_0)^\beta,$$

where the functions $r_\beta^{(k)}$ satisfy $\lim_{\mathbf{x} \rightarrow \mathbf{x}_0} r_\beta^{(k)}(\mathbf{x}) = 0$. Fix $k \in \mathbb{N}$, and take $R_k > 0$ so that $|r_\beta^{(k)}(\mathbf{x})| \leq 1/2$ for every $|\mathbf{x} - \mathbf{x}_0| \leq R_k$. It follows that

$$|f(\mathbf{x}) - P_k(\mathbf{x} - \mathbf{x}_0)| \leq C_k |\mathbf{x} - \mathbf{x}_0|^k$$

for every $|\mathbf{x} - \mathbf{x}_0| \leq R_k$, i.e., $f \in C^k(\mathbf{x}_0)$ for every $k \in \mathbb{N}$.

The key result of Jaffard is the following, see [15, Theorem 2]. Let $\psi: \mathbb{R}^d \rightarrow \mathbb{R}$ be a mother wavelet with derivatives of order $N > \alpha$ decaying faster than the inverse of any polynomial, and define

$$\psi_{j,k}(\mathbf{x}) = 2^{jd/2} \psi(2^j \mathbf{x} - \mathbf{k}), \quad j \in \mathbb{Z}, \quad \mathbf{k} \in \mathbb{Z}^d,$$

If $f \in C^\alpha(\mathbf{x}_0)$, then its L^2 -normalized wavelet coefficients

$$c_{j,k} = (f, \psi_{j,k})_{L^2}$$

for wavelets $\psi_{j,k}$ whose support is localized around \mathbf{x}_0 exhibit a characteristic decay

$$(4) \quad |c_{j,k}| \lesssim 2^{-j(\alpha+d/2)},$$

which yields a characterization of $C^\alpha(\mathbf{x}_0)$.

2.2. Construction of Samplets. Samplets are localized discrete signed measures, which exhibit vanishing moments. We briefly recall their underlying concepts as introduced in [11]. Let $X := \{\mathbf{x}_1, \dots, \mathbf{x}_N\} \subset \Omega \subset \mathbb{R}^d$ denote a set of data sites, and consider the associated Dirac- δ -distributions $\delta_{\mathbf{x}_1}, \dots, \delta_{\mathbf{x}_N} \in \mathcal{C}(\Omega)'$. Here and in what follows, $\mathcal{C}(\Omega)$ denotes the space of continuous functions and $\mathcal{C}(\Omega)'$ its topological dual space. We recall that the Dirac- δ -distributions are defined by the property

$$(\delta_{\mathbf{x}_i}, f)_\Omega := \delta_{\mathbf{x}_i}(f) = f(\mathbf{x}_i)$$

for all $f \in \mathcal{C}(\Omega)$. For a given function f , we consider the data values $f_i := (f, \delta_{\mathbf{x}_i})_\Omega$, $i = 1, \dots, N$, which amount to the available information about f . The span of the Dirac- δ -distributions, $\mathcal{X}' := \text{span}\{\delta_{\mathbf{x}_1}, \dots, \delta_{\mathbf{x}_N}\} \subset \mathcal{C}(\Omega)'$, naturally forms a Hilbert space with inner product defined as

$$\langle u, v \rangle_{\mathcal{X}'} := \sum_{i=1}^N u_i v_i, \quad \text{with } u = \sum_{i=1}^N u_i \delta_{\mathbf{x}_i} \text{ and } v = \sum_{i=1}^N v_i \delta_{\mathbf{x}_i}.$$

This choice of inner product is motivated by considering the space \mathcal{X}' in the context of Banach frames. For the details, we refer to [2].

For the construction of samplelets, we introduce a multiresolution analysis for \mathcal{X}' . A multiresolution analysis is a nested sequence of subspaces $\mathcal{X}'_0 \subset \mathcal{X}'_1 \subset \dots \subset \mathcal{X}'_J := \mathcal{X}'$. We assume that each subspace is spanned by a basis $\Phi_j := \{\varphi_{j,k}\}_k$, i.e., $\mathcal{X}'_j = \text{span } \Phi_j$. Particularly, each *scaling distribution* $\varphi_{j,k}$ can be expressed as a linear combination of Dirac- δ -distributions. Due to the nested structure, the space \mathcal{X}'_{j+1} can be orthogonally decomposed into $\mathcal{X}'_{j+1} = \mathcal{X}'_j \oplus \mathcal{S}'_j$, where the detail space \mathcal{S}'_j is equipped with an orthonormal basis $\Sigma_j := \{\sigma_{j,k}\}_k$. Recursively applying this decomposition yields the *samplelet basis* $\Sigma_J = \Phi_0 \cup \bigcup_{j=0}^{J-1} \Sigma_j$, which serves as a basis for \mathcal{X}' .

To enable data feature detection, samplelets can be constructed to satisfy vanishing moments for a given set of primitives. Specifically, we consider here polynomials $p \in \mathcal{P}_q(\Omega)$ of total degree less or equal than q and require that

$$(5) \quad (\sigma_{j,k}, p)_\Omega = 0 \quad \text{for all } p \in \mathcal{P}_q(\Omega).$$

The multilevel hierarchy underlying the construction of samplelets is obtained by clustering the Dirac- δ -distributions based on the distance of their supports. This is achieved by a hierarchical cluster tree \mathcal{T} for the set of data sites X .

Definition 2.4. Let $\mathcal{T} = (V, E)$ be a tree with vertex set V and edge set E . The set of leaves of \mathcal{T} is defined as $\mathcal{L}(\mathcal{T}) := \{\tau \in V : \tau \text{ has no children}\}$. The tree \mathcal{T} is called a cluster tree for the set X if the root node corresponds to X , and every non-leaf node $\tau \in V \setminus \mathcal{L}(\mathcal{T})$ is the disjoint union of its children. The level j_τ of a node $\tau \in V$ is the number of edges in the unique path from the root to τ and the depth J of \mathcal{T} is the maximum level of all nodes. For each $\tau \in V$, the bounding box B_τ is defined as the smallest axis-aligned dyadic cuboid containing all points associated with τ . Finally, we set $\text{diam}(\tau) := \max_{\mathbf{x}_i, \mathbf{x}_j \in \tau} \|\mathbf{x}_i - \mathbf{x}_j\|_2$.

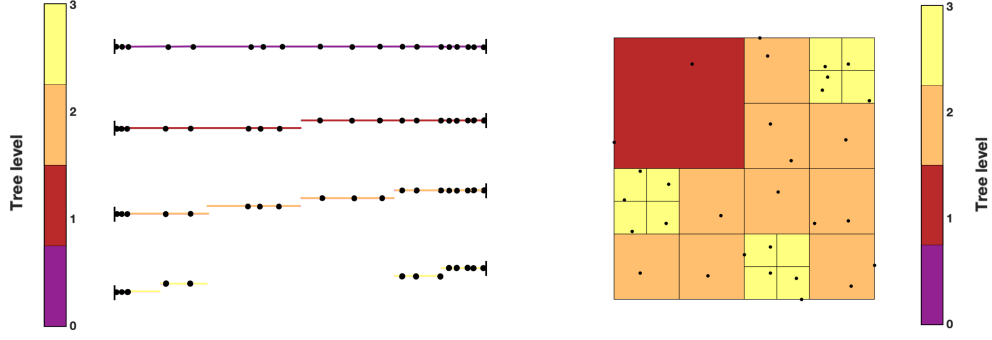
Differently from the original construction in [11], which relies on balanced binary trees, we rather consider 2^d -trees to hierarchically partition the set of data sites. For the reader's convenience, we recall the definition.

Definition 2.5. A cluster tree \mathcal{T} for X with depth J is called a 2^d -tree, if the cluster τ has exactly 2^d children whenever $j_\tau < J$. We further say that \mathcal{T} is balanced if there holds

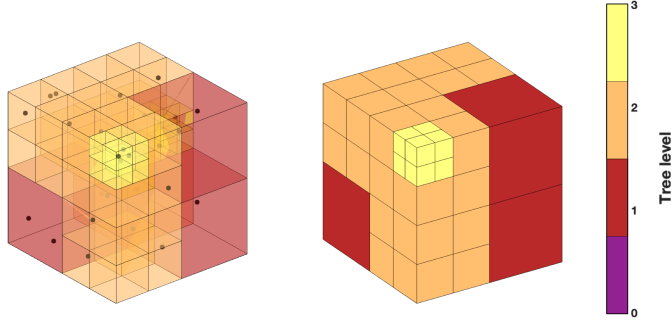
$$(6) \quad \#\tau \sim N 2^{-j_\tau d},$$

where $\#\tau$ denotes the cardinality of τ .

A 2^d -tree can easily be constructed by geometric clustering, where each non-leaf node is recursively subdivided into 2^d child clusters by dyadic subdivision of the edges of the bounding box of X , see Figure 1 for an illustration. For quasi-uniform sets X in the sense that the fill-distance of X is similar to the separation radius of X , this approach even yields a balanced 2^d -tree. To avoid technicalities, we will in the following therefore assume that X is quasi-uniform.



(A) Binary tree (left) and quadtree (right).



(B) Octree.

FIGURE 1. Examples of 2^d -trees in dimensions $d = 1, 2, 3$.

For a balanced 2^d -tree, we obtain $J \sim d \log_2 N$ levels. At each level j , all N points are split into 2^{jd} clusters, and the division can be performed with linear cost. Hence, the overall cost for the construction of the 2^d -tree is $\mathcal{O}(JN) = \mathcal{O}(N \log N)$ in this case. If further structural details are available on X , e.g., in case that X refers to the pixels of an image, and the level J is known a-priorily, the cost for the construction of the cluster tree reduces to $\mathcal{O}(N)$. This is facilitated by subdividing the bound box of X into 2^{Jd} congruent cuboids and attributing each element of X to one of these cuboids. Afterwards, 2^d cuboids are successively combined to obtain a cluster tree.

Next, we construct a sample basis based on the hierarchical structure of the cluster tree. Scaling distributions $\Phi_j^\tau = \{\varphi_{j,k}^\tau\}$ and samplelets $\Sigma_j^\tau = \{\sigma_{j,k}^\tau\}$ of a given node $\tau \in \mathcal{T}$ are represented as linear combinations of the gathered scaling distributions Φ_{j+1}^τ of all of τ 's children. The refinement relation for the two-scale transform between basis elements is given by

$$(7) \quad \varphi_{j,k}^\tau = \sum_{\ell=1}^{n_{j+1}^\tau} q_{j,\Phi,\ell,k}^\tau \varphi_{j+1,\ell}^\tau \quad \text{and} \quad \sigma_{j,k}^\tau = \sum_{\ell=1}^{n_{j+1}^\tau} q_{j,\Sigma,\ell,k}^\tau \varphi_{j+1,\ell}^\tau,$$

where $n_{j+1}^\tau := \#\Phi_{j+1}^\tau$. In matrix form, this is compactly expressed as

$$[\Phi_j^\tau, \Sigma_j^\tau] := \Phi_{j+1}^\tau Q_j^\tau = \Phi_{j+1}^\tau [Q_{j,\Phi}^\tau, Q_{j,\Sigma}^\tau].$$

To obtain samplelets enjoying vanishing moments, the filter coefficients \mathbf{Q}_j^τ are computed by the QR decomposition of the transpose of the moment matrix

$$\mathbf{M}_{j+1}^\tau := [(\mathbf{x}^\alpha, \Phi_{j+1}^\tau)_\Omega]_{|\alpha| \leq q}.$$

In particular, this guarantees the orthonormality of the resulting basis. For all the details, we refer to [11, Section 3.2].

In the following, we assume a global, levelwise indexing of the samplelets and simply write $\sigma_{j,k}$ for a samplelet on level j . Furthermore, we will not distinguish between samplelets and scaling distributions at level 0 and refer to either of them as $\sigma_{0,k}$.

Remark 2.6. Every samplelet $\sigma_{j,k} \in \mathcal{X}'_j$, $j = 0, \dots, J$, is a linear combination of the Dirac- δ -distributions $\delta_{\mathbf{x}_1}, \dots, \delta_{\mathbf{x}_N}$ and can thus be written as

$$\sigma_{j,k} = \sum_{\ell=1}^N \omega_{j,k}^{(\ell)} \delta_{\mathbf{x}_\ell}.$$

We denote the coefficient vector of $\sigma_{j,k}$ by $\boldsymbol{\omega}_{j,k} = [\omega_{j,k}^{(\ell)}]_{\ell=1}^N$ and notice that $\omega_{j,k}^{(\ell)} = 0$ whenever $\mathbf{x}_\ell \notin \text{supp } \sigma_{j,k}$.

Moreover, there holds $\|\boldsymbol{\omega}_{j,k}\|_2 = 1$ and, using Cauchy-Schwarz inequality,

$$(8) \quad \|\boldsymbol{\omega}_{j,k}\|_1 \leq \sqrt{\#\tau} \|\boldsymbol{\omega}_{j,k}\|_2 = \sqrt{\#\tau}.$$

see also [11, Remark 3.8].

Remark 2.7. Samplelets can be interpreted as distributional wavelets. Consider the case where $\Omega = [0, 1]^d$, then the samplelet $\sigma_{j,k}$ with support contained in $Q_{\mathbf{p},j} := \mathbf{p} + 2^{-j}\Omega$, where $\mathbf{p}_m \in 2^{-j}\{0, \dots, 2^j - 1\}$ for $m = 1, \dots, d$, acts on $f \in \mathcal{C}(\Omega)$ by

$$(\sigma_{j,k}, f)_\Omega = \sum_{\ell=1}^N \omega_{j,k}^{(\ell)} f(\mathbf{x}_\ell).$$

By writing $\mathbf{x}_\ell = \mathbf{p} + 2^{-j}\mathbf{y}_\ell$, $\mathbf{y}_\ell \in \Omega$, we find

$$(9) \quad (\sigma_{j,k}, f)_\Omega = \sum_{\ell=1}^N \omega_{j,k}^{(\ell)} f(2^{-j}\mathbf{y}_\ell + \mathbf{p}) = 2^{jd/2} \sum_{\ell=1}^N \omega_{j,k}^{(\ell)} (T_{-\mathbf{p}} D_{-j} f)(\mathbf{y}_\ell),$$

where $T_{\mathbf{p}} f = f(\cdot - \mathbf{p})$, and $D_j f = 2^{jd/2} f(2^j \cdot)$, $j \in \mathbb{Z}$, are the translation and the L^2 -normalized dilation operator, respectively. By definition of translations and dilations of distributions, we may rephrase (9) as

$$(10) \quad (\sigma_{j,k}, f)_\Omega = 2^{jd/2} \left(D_j T_{\mathbf{p}} \sum_{\ell=1}^N \omega_{j,k}^{(\ell)} \delta_{\mathbf{y}_\ell}, f \right)_\Omega,$$

which stresses that each samplelet can be considered a distributional mother wavelet.

2.3. Fast samplelet transform. To change between the basis of Dirac- δ -distributions and the samplelet basis, we employ the fast samplelet transform or its inverse, respectively. Given the data points $\{(\mathbf{x}_i, y_i)\}_{i=1}^N$, we set

$$y_i = f_i^\Delta := (\delta_{\mathbf{x}_i}, f)_\Omega,$$

for some possibly unknown function $f: \Omega \rightarrow \mathbb{R}$. We identify f by the functional

$$f = \sum_{i=1}^N f_i^\Delta \delta_{\mathbf{x}_i},$$

which takes the form

$$f = \sum_{i=1}^N f_i^\Sigma \sigma_i$$

in the samplelet basis. We refer to [2] for rigorous derivation and a functional analytic motivation of this functional.

The fast samplelet transform maps the coordinate vector $\mathbf{f}^\Delta = [f_i^\Delta]_{i=1}^N$ in the basis of Dirac- δ -distributions to the coordinate vector $\mathbf{f}^\Sigma = [f_i^\Sigma]_{i=1}^N$ in the samplelet basis, according to the relation $\mathbf{f}^\Sigma = \mathbf{T} \mathbf{f}^\Delta$, where $\mathbf{T} \in \mathbb{R}^{N \times N}$ is the orthogonal matrix containing the filter coefficients from (7). We remark that the matrix T is not assembled in practice and that the fast samplelet transform can be performed recursively with cost $\mathcal{O}(N)$. The same holds true for the inverse transform. For the implementation details, see [11, Section 4].

3. LOCAL SMOOTHNESS DETECTION

In this section, we present the theoretical foundations for detecting local regularity using samplelets. Building on the pointwise Hölder exponent framework introduced for wavelets in [16], we establish analogous decay estimates for samplelet coefficients. The motivation for adopting a pointwise approach lies in the structure of the samplelet tree. Specifically, for a fixed $\mathbf{x}_0 \in \Omega$ consider the unique leaf of the cluster tree that contains \mathbf{x}_0 . Consider then the branch joining that leaf to the corresponding clusters at each level j . As the level j increases, the number of data sites within each cluster decreases. Thus, descending along a branch corresponds to analyzing the function f in a successively decreasing neighborhood around the point \mathbf{x}_0 . Our main result is for $C^\alpha(\mathbf{x}_0)$ classes.

Theorem 3.1. *Let $\mathbf{x}_0 \in \Omega$ and $f \in C^\alpha(\mathbf{x}_0)$, $\alpha \geq 0$. Assume that (5) holds for $q \geq \lfloor \alpha \rfloor$. Then, for every cluster τ that contains \mathbf{x}_0 , we have*

$$(11) \quad |(\sigma_{j,k}, f)| \lesssim \text{diam}(\tau)^\alpha \sqrt{\#\tau}.$$

In particular, for $\Omega = [0, 1]^d$ and balanced 2^d -trees, there holds

$$(12) \quad |(\sigma_{j,k}, f)_\Omega| \lesssim \sqrt{Nd^\alpha} 2^{-j(\alpha+d/2)},$$

where N is the number of data sites.

Proof. Let $\mathbf{x}_0 \in \Omega$ and τ be any cluster containing \mathbf{x}_0 with $\text{diam}(\tau) \leq R$, where R is the constant in the definition of the microlocal space $C^\alpha(\mathbf{x}_0)$. We can write the samplelet $\sigma_{j,k}$ as a linear combination of Dirac- δ -distributions, say $\sigma_{j,k} = \sum_{\ell=1}^{\#\tau} \omega_{j,k}^{(\ell)} \delta_{\mathbf{x}_\ell}$, where $\{\mathbf{x}_1, \dots, \mathbf{x}_{\#\tau}\}$ are the data sites contained in τ .

Let P be a polynomial satisfying (1). By the vanishing moments property (5), there holds

$$(\sigma_{j,k}, f)_\Omega = (\sigma_{j,k}, f - P(\cdot - \mathbf{x}_0))_\Omega = \sum_{\ell=1}^{\#\tau} \omega_{j,k}^{(\ell)} (f(\mathbf{x}_\ell) - P(\mathbf{x}_\ell - \mathbf{x}_0)),$$

such that (1) yields

$$\begin{aligned} |(\sigma_{j,k}, f)_\Omega| &\leq \sum_{\ell=1}^{\#\tau} |\omega_{j,k}^{(\ell)}| |f(\mathbf{x}_\ell) - P(\mathbf{x}_\ell - \mathbf{x}_0)| \lesssim \sum_{\ell=1}^{\#\tau} |\omega_{j,k}^{(\ell)}| |\mathbf{x}_\ell - \mathbf{x}_0|^\alpha \\ &\leq \sqrt{\#\tau} \left(\sum_{\ell=1}^{\#\tau} |\omega_{j,k}^{(\ell)}|^2 \right)^{1/2} \text{diam}(\tau)^\alpha \leq \text{diam}(\tau)^\alpha \sqrt{\#\tau}, \end{aligned}$$

where we also used Remark 2.6. This proves (11). In the framework of balanced 2^d -trees, $\#\tau \sim 2^{-jd}N$ and $\text{diam}(\tau) = \sqrt{d}2^{-j}$. Inserting these information into (11) proves (12). \square

Remark 3.2. *Let us comment on the decay of coefficients of a function f that is infinitely many times differentiable in a point \mathbf{x}_0 , in the setting of balanced 2^d -trees. By Remark 2.3, there holds $f \in C^m(\mathbf{x}_0)$ for every $m \in \mathbb{N}$. For every fixed $q \geq 1$ such that (5) holds, we have*

$$|(\sigma_{j,k}, f)_\Omega| \leq \sqrt{Nd^{q+1}}2^{-j(q+1+d/2)},$$

following by Remark 2.3 and Theorem 3.1.

The microlocal space $C^\alpha(\mathbf{x}_0)$ contains the usual Hölder space of $\lfloor \alpha \rfloor$ -times differentiable functions with $(\alpha - \lfloor \alpha \rfloor)$ -Hölder continuous derivatives of order $\lfloor \alpha \rfloor$, as explained in Remark 2.2. Hence, we also obtain the decay of sample coefficients of locally Hölder continuous functions as a consequence of Theorem 3.1.

Corollary 3.3. *Let $0 < \vartheta \leq 1$, $m \in \mathbb{N}$ and $\mathbf{x}_0 \in \Omega$ and consider $f \in C^{m,\vartheta}(B_R(\mathbf{x}_0))$. Then, assuming that (5) holds for $q \geq m$, we have that*

$$(13) \quad |(\sigma_{j,k}, f)| \lesssim \text{diam}(\tau)^{\vartheta+m} \sqrt{\#\tau}.$$

In particular, in the framework of balanced 2^d -trees, where $\Omega = [0, 1]^d$,

$$|(\sigma_{j,k}, f)_\Omega| \lesssim \sqrt{Nd^{\vartheta+m}}2^{-j(\vartheta+m+d/2)},$$

where N is the number of data sites.

Proof. By Remark 2.2, $f \in C^{k+\vartheta}(\mathbf{x}_0)$, and (13) follows by applying (11) with $\alpha = k + \vartheta$. \square

We can also infer the decay of the sample coefficients for functions in Sobolev-Slobodeckij spaces [6], whose definition is reported below. For the purpose of this work, we may consider $\Omega' \subset \mathbb{R}^d$ to be a closed ball of conveniently small radius. Let $1 \leq p < \infty$, $0 < \rho < 1$ and $f \in L^p(\Omega')$. The *Slobodeckij- or Gagliardo-seminorm* of f is

$$[f]_{\rho,p,\Omega'} = \left(\int_{\Omega'} \int_{\Omega'} \frac{|f(\mathbf{x}) - f(\mathbf{y})|^p}{|\mathbf{x} - \mathbf{y}|^{\rho p + d}} d\mathbf{x} d\mathbf{y} \right)^{1/p}.$$

Let $s > 0$. We say that f is in the *Sobolev-Slobodeckij space* $W^{s,p}(\Omega')$ if f is in the Sobolev space $W^{\lfloor s \rfloor,p}(\Omega')$, and

$$\max_{|\beta|=\lfloor s \rfloor} [\partial^\beta f]_{s-\lfloor s \rfloor,p,\Omega'} < \infty.$$

Then,

$$(14) \quad \|f\|_{W^{s,p}(\Omega')} = \|f\|_{W^{\lfloor s \rfloor,p}(\Omega')} + \max_{|\beta|=\lfloor s \rfloor} [\partial^\beta f]_{s-\lfloor s \rfloor,p,\Omega'}$$

defines a Banach space norm on $W^{s,p}(\Omega')$. In particular, we see by (14) that $W^{s,p}(\Omega') \subseteq W^{\lfloor s \rfloor,p}(\Omega')$. Moreover, Sobolev-Slobodeckij spaces coincide with the usual Sobolev spaces when s is an integer, i.e., $W^{s,p}(\Omega') = W^{m,p}(\Omega')$ if $s = m \in \mathbb{N}$.

By the Sobolev embedding theorem [6, Theorem 4.58] and Remark 2.2, we retrieve the following embedding of Sobolev-Slobodeckij spaces and microlocal spaces.

Lemma 3.4. *Assuming $s > d/p$, the following statements hold.*

- (i) *If $s - d/p \notin \mathbb{N}$, then $W^{s,p}(\Omega') \subseteq \mathcal{C}^{\lfloor s-d/p \rfloor, \vartheta}(\Omega')$ for every $0 < \vartheta < s - d/p - \lfloor s - d/p \rfloor$.*
- (ii) *If $s - d/p \in \mathbb{N}$, then $W^{s,p}(\Omega') \subseteq \mathcal{C}^{s-d/p-1, \vartheta}(\Omega')$ for every $0 < \vartheta < 1$.*

In particular, for every $\varepsilon > 0$ sufficiently small, there holds

$$W^{s,p}(\Omega') \subseteq C^{s-\frac{d}{p}-\varepsilon}(\mathbf{x}_0).$$

Proof. Items (i) and (ii) are precisely the content of [6, Theorem 4.58]. If $\mathbf{x}_0 \in \Omega'$ and Ω' is a closed ball containing \mathbf{x}_0 with conveniently small radius, the inclusion $C^{k,\vartheta}(\Omega') \subseteq C^{k+\vartheta}(\mathbf{x}_0)$ holds and the last claim follows by items (i) and (ii). \square

Finally, the following result follows by applying Theorem 3.1 to a function f under the assumptions of this section.

Corollary 3.5. *Let $\mathbf{x}_0 \in \Omega \subseteq \Omega$ and let Ω' be a closed ball centered in \mathbf{x}_0 with conveniently small radius. Let $f \in W^{s,p}(\Omega')$, with $1 \leq p < \infty$ and $s > d/p$. If (5) holds for $q \geq \lfloor s-d/p \rfloor$, we have that*

$$|(\sigma_{j,k}, f)| \lesssim \text{diam}(\tau)^{s-d/p-\varepsilon} \sqrt{\#\tau}$$

for every $\varepsilon < s - d/p - \lfloor s - d/p \rfloor$. In particular, in the framework of balanced 2^d -trees, if $p = 2$, we have that for every $\varepsilon < s - d/2 - \lfloor s - d/2 \rfloor$ there holds

$$|(\sigma_{j,k}, f)_\Omega| \lesssim \sqrt{Nd^{s-d/2-\varepsilon}} 2^{-j(s-\varepsilon)},$$

where N is the number of data sites.

4. SAMPLETS FOR LOCAL SMOOTHNESS DETECTION

In this section, we apply the developed framework to analyze the local smoothness properties of a given function f using samplets. For the set of data sites $X = \{\mathbf{x}_1, \dots, \mathbf{x}_N\}$, we first partition X through a 2^d -tree. Then, we apply the fast samplet transform $\mathbf{f}^\Sigma = \mathbf{T}\mathbf{f}^\Delta$ to the vector $\mathbf{f}^\Delta = [f(\mathbf{x}_1), \dots, f(\mathbf{x}_N)]$, as explained in Section 2. Finally, we fit the decay rates of the samplet coefficients along each branch of the tree. To this end, we traverse the 2^d -tree using a depth-first search (DFS), see [29]. For a fixed branch $\mathbf{r} = [\tau_0, \dots, \tau_J]$ of the tree, let $\mathbf{e}_\mathbf{r} = [e_0^\mathbf{r}, \dots, e_J^\mathbf{r}]$ denote the vector of the cluster-wise Euclidean norms of the samplet coefficients along this branch. Precisely,

$$e_j^\mathbf{r} = \|\mathbf{f}^\Sigma|_{\tau_j}\|_2, \quad j = 0, \dots, J,$$

where $\mathbf{f}^\Sigma|_{\tau_j}$ denotes the subvector of \mathbf{f}^Σ whose entries correspond to the coefficients of the samplets that are supported on the cluster τ_j . Similarly to $\mathbf{e}_\mathbf{r}$, we define $\mathbf{b}_\mathbf{r} = [b_0^\mathbf{r}, \dots, b_J^\mathbf{r}]$ as the vector of diameters of the bounding boxes of the nodes along the branch, where $b_j^\mathbf{r}$ denotes the diameter of the bounding box of the node at level j . An illustration of this setup is provided in Figure 2.

Exploiting the fact that the diameter of a node at level j in a balanced 2^d -tree satisfies

$$b_j^\mathbf{r} \sim 2^{-j},$$

and using the previously proven Theorem 3.1, we estimate the local Hölder exponent α by fitting the decay of the samplet coefficients $\mathbf{e}_\mathbf{r}$ according to the model

$$e_j^\mathbf{r} \approx c (b_j^\mathbf{r})^{\alpha+d/2}.$$

Taking the logarithm on both sides yields the linearized model

$$(15) \quad \log e_j^\mathbf{r} \approx \log c + \left(\alpha + \frac{d}{2} \right) \log b_j^\mathbf{r}.$$

This leads to a linear least-squares problem of the form

$$(16) \quad \mathbf{A}\mathbf{x} = \mathbf{y},$$

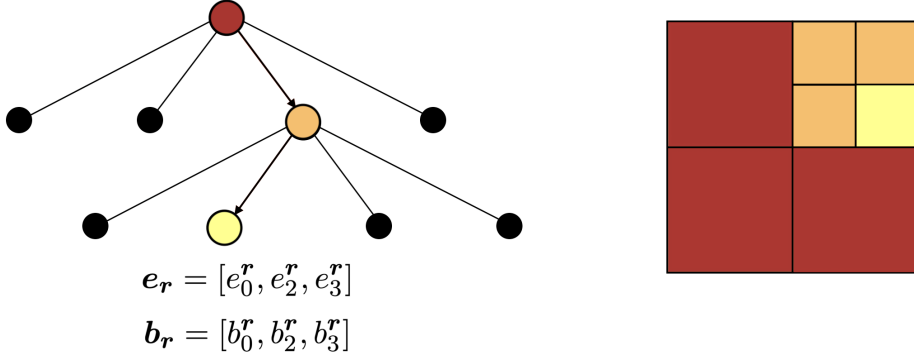


FIGURE 2. Illustration of a fixed branch in the samplet tree (left) and its corresponding nested regions in the computational domain (right). Each node along the branch is associated with the Euclidean norms of the samplet coefficients and a bounding box whose diameter reflects the local resolution.

where

$$\mathbf{A} = \begin{bmatrix} 1 & \log b_0^r \\ \vdots & \vdots \\ 1 & \log b_J^r \end{bmatrix} \in \mathbb{R}^{(J+1) \times 2}, \quad \mathbf{x} = \begin{bmatrix} \log c \\ \alpha + d/2 \end{bmatrix} \in \mathbb{R}^2, \quad \mathbf{y} = \begin{bmatrix} \log e_0^r \\ \vdots \\ \log e_J^r \end{bmatrix} \in \mathbb{R}^{J+1}.$$

To solve (16), we apply the reduced QR decomposition

$$\mathbf{A} = \mathbf{Q}\mathbf{R},$$

where $\mathbf{Q} \in \mathbb{R}^{(J+1) \times 2}$ has orthonormal columns and $\mathbf{R} \in \mathbb{R}^{2 \times 2}$ is upper triangular. Using the orthogonality of \mathbf{Q} , we rewrite the least-squares residual as

$$\|\mathbf{A}\mathbf{x} - \mathbf{y}\|_2 = \|\mathbf{Q}\mathbf{R}\mathbf{x} - \mathbf{y}\|_2 = \|\mathbf{R}\mathbf{x} - \mathbf{Q}^\top \mathbf{y}\|_2.$$

Letting $\mathbf{z} = \mathbf{Q}^\top \mathbf{y}$, we solve the upper-triangular system

$$\mathbf{R}\mathbf{x} = \mathbf{z}$$

to obtain the least-squares estimate of the parameters $\log c$ and $(\alpha + d/2)$.

Remark 4.1. Let us comment on the detection of points or regions where we consider functions to be infinitely many times differentiable. The polynomial degree q , see (5), represents the maximum order of C^α regularity that can be detected by our algorithm. Roughly speaking, it plays the role of “infinity”. In regions where the signal is smooth, at least the finest-scale samplet coefficient e_J^r drops to a negligible value. To detect this scenario before performing the linear regression (15), we compute the ratio $e_J^r / \|\mathbf{e}^r\|_2$. If this ratio is close to machine precision, we conclude that no finer resolution is needed. In this case, we directly assign the branch the maximal Hölder exponent $\alpha + d/2 \leftarrow q + 1$.

The smoothness class detection with samplets is summarized in Algorithm 2. In synthesis, we detect local smoothness along each branch of the samplet tree \mathcal{T} in three steps. First, we build the map **branchData** by walking down every branch and collecting two parallel lists: the norms of the samplet coefficients and the diameters of their bounding boxes. Next, for each branch, we fit a line to the logarithm of coefficient norms versus the logarithm of box diameters and record the resulting decay rate in the map **branchSlopes**. Finally, we assign the local regularity according to Theorem 3.1.

Algorithm 1 DFS for Collecting Branch Data

Input: Samplet tree \mathcal{T} , samplet transformed data \mathbf{f}^Σ .
Output: map **branchData** associating to each branch $\mathbf{r} \subset \mathcal{T}$ a pair of vectors $[e_{\mathbf{r}}, b_{\mathbf{r}}]$.

```

1: function TRAVERSEANDCOLLECT( $\tau, \mathbf{r}$ )
2:    $e_{\mathbf{r}} \leftarrow [e_{\mathbf{r}}, e_{j_{\tau}}^{\mathbf{r}}]$ 
3:    $b_{\mathbf{r}} \leftarrow [b_{\mathbf{r}}, b_{j_{\tau}}^{\mathbf{r}}]$ 
4:    $\mathbf{r} \leftarrow [\mathbf{r}, \tau]$ 
5:   if  $\tau$  is a leaf then
6:     branchData $[\mathbf{r}] \leftarrow [e_{\mathbf{r}}, b_{\mathbf{r}}]$  ▷ If leaf, save coefficients and diameters
7:   else
8:     for  $\tau_{\text{child}}$  in children( $\tau$ ) do
9:       TRAVERSEANDCOLLECT( $\tau_{\text{child}}, \mathbf{r}$ ) ▷ Recursively visit children
10:    end for
11:  end if
12: end function
13:  $e_{\mathbf{r}} \leftarrow []$ 
14:  $b_{\mathbf{r}} \leftarrow []$ 
15: TRAVERSEANDCOLLECT( $\tau = X, \mathbf{r} = []$ ) ▷ Start DFS from root
16: return branchData

```

Algorithm 2 Compute Hölder Exponents

Input: map **branchData**, as produced by Algorithm 1
Output: map **branchSlope**, associating each branch $\mathbf{r} \subset \mathcal{T}$ with the samplet coefficients'

```

1:   decay  $(\alpha + d/2)$ .
2: branchSlope  $\leftarrow \{\}$ 
3: for  $\mathbf{r}$  in branchData do
4:   Fit a line to  $\log(e_{\mathbf{r}})$  to get the slope  $(\alpha + d/2)$  using (15)
5:   branchSlope $[\mathbf{r}] \leftarrow (\alpha + d/2)$ 
6: end for
7: return branchSlope

```

5. NUMERICAL RESULTS

In this section, we apply the proposed method to local regularity detection in one-, two-, and three-dimensional signals, on both gridded and scattered data. The experiments have been performed on a MacBook Pro with an Apple M2 Max processor and 32 GB of main memory. In the first experiment, we employ samplet transform with $q + 1 = 5$ vanishing moments, see (5), whereas we employ samplet $q + 1 = 3$ vanishing moments for the remaining experiments, classifying signals as locally smooth when they are at least five and three times differentiable, respectively.

In the experiments, if τ is a leaf node, we detect the same local Hölder exponent for every sample $(\mathbf{x}, f(\mathbf{x}))$ with $\mathbf{x} \in \tau$. For this reason, we introduce a mild abuse of language and say that our algorithm assigns the microlocal space C^α to the cluster τ .

5.1. One-dimensional setting. First, we consider a signal on $\Omega = [-1, 1]$, which presents jumps and corners. Specifically, we consider

$$f_1(x) = \begin{cases} 6 & \text{if } x < -0.4, \\ 0.1 \cdot |20x + 9| + 6 & \text{if } -0.4 \leq x < -0.35, \\ 0.1 \cdot |20x + 5| + 6 & \text{if } -0.35 \leq x < -0.15, \\ 0.1 \cdot |20x + 1| + 6 & \text{if } -0.15 \leq x < -0.05, \\ 6 + \sin(20\pi x) & \text{if } -0.05 \leq x < 0.55, \\ 4 - 20|x - 0.7|(x - 0.7) & \text{if } 0.55 \leq x \leq 1 \end{cases}$$

Near jumps, the signal is locally 0-Hölder continuous, i.e., $f \in C^\alpha(x_0)$ with $\alpha = 0$, whereas the regularity increases up to $\alpha = 1$ near corners. By Theorem 3.1, we expect a rate of decay of order slightly smaller than $\frac{1}{2}$ at jumps and slightly smaller than $\frac{3}{2}$ at corners. In this experiment, we consider a random uniformly distributed set of one million points. The result is shown in Figure 3. The top row of the figure shows the given signal, while the

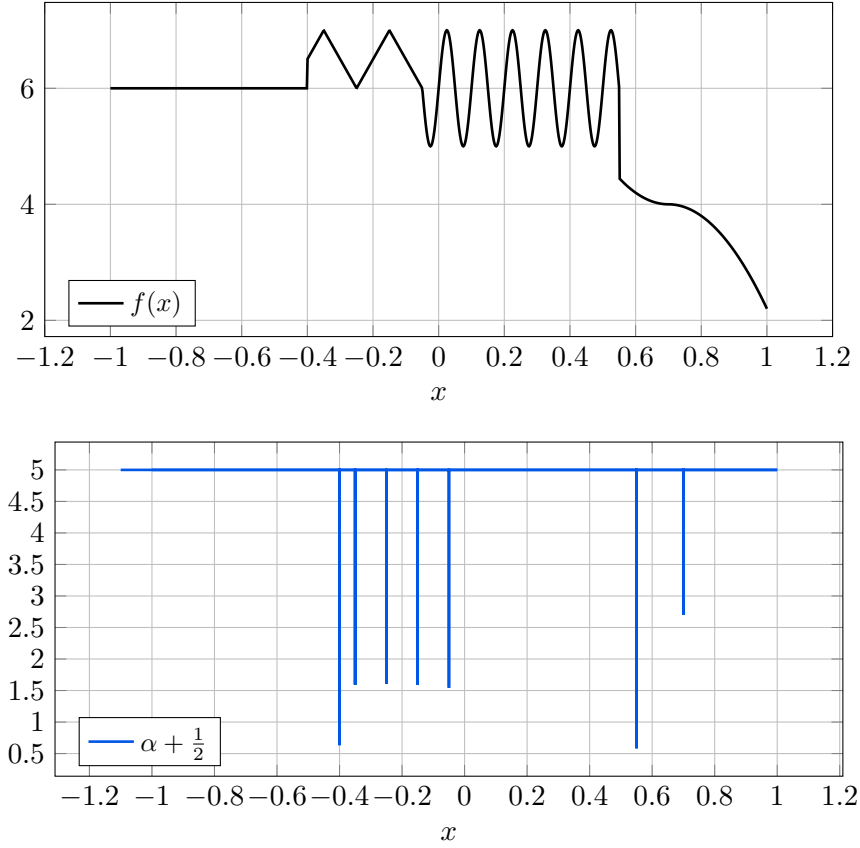


FIGURE 3. Top: Original function f plot. Bottom: Local Hölder exponents. Our algorithm assigns the microlocal space $C^{0.5-\frac{d}{2}} = C^0$ to clusters intersecting a jump; the space $C^{1.5-\frac{d}{2}} = C^1$ to clusters intersecting the corners; finally, it assigns $C^{2.5-\frac{d}{2}} = C^2$ to clusters intersecting singularities on the second derivative we detect.

bottom row shows the obtained smoothness chart. As can be seen, all types of singularities as well as the smooth regions are correctly identified.

5.2. Two-dimensional setting. We consider bivariate signals defined on the unit square $\Omega = [0, 1]^2$. First, we analyze the standard example of a function with a corner discontinuity

$$h(x, y) = |x - y|,$$

see Figure 4 for the results. A further, more intriguing, question is to understand whether samplet analysis of singularities is sensitive to pathologies arising in the multivariate framework. For instance, the function

$$(17) \quad g(x, y) = \frac{1}{2} \left(\frac{y - 0.25}{\sqrt{(x - 0.25)^2 + (y - 0.25)^2}} + \frac{(x - 0.75)^2(y - 0.75)}{(x - 0.75)^2 + (y - 0.75)^2} \right),$$

merges two classical examples in mathematical analysis of bivariate functions. In both the points $(0.25, 0.25)$ and $(0.75, 0.75)$, all the directional derivatives exist, but g is not continuous in $(0.25, 0.25)$ and not differentiable in $(0.75, 0.75)$. The results are displayed in Figure 5. In this numerical experiment, each function is sampled on a uniform $2^{11} \times 2^{11}$ grid.

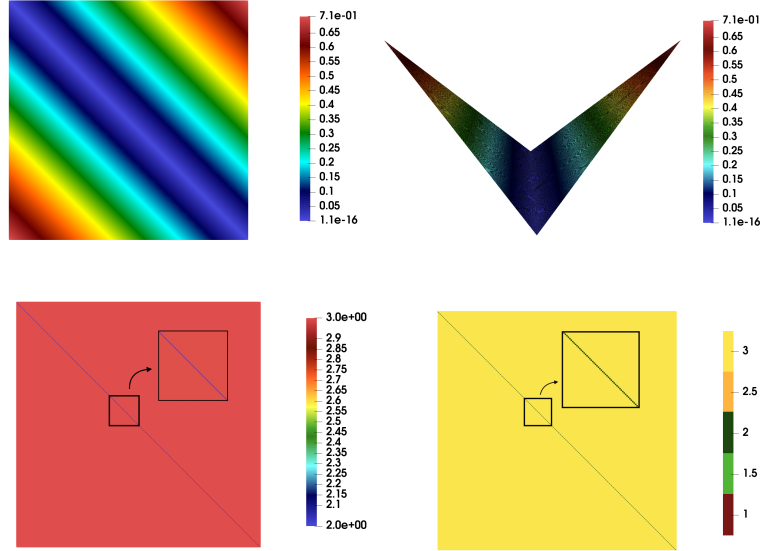


FIGURE 4. Top: Two-dimensional (left) and three-dimensional (right) plots of the corner function on the unit square Ω . Bottom: Local Hölder exponents, displayed with linear (left) and structured (right) colormaps. Our algorithm assigns the space $C^{2-\frac{d}{2}} = C^1$ to clusters intersecting the corner.

The results are in agreement with Theorem 3.1. In the first example, near the ridge, the decay rate is 2, implying local Hölder exponents of 1. For the second experiment, see Figure 5, we detect a Hölder exponent of 0 at the point $(0.25, 0.25)$, where the function g in (17) is not continuous, and a Hölder exponent of 1 in $(0.75, 0.75)$, where it is continuous, but not differentiable. Therefore, our results agree with the classical notion of differentiability, meaning that the existence of the partial derivatives in a point does not affect the local Hölder exponent detected using samplets.

5.3. Edge detection. Edge detection is also a powerful tool for the automatic identification of regions of interest or distinct profiles within an image. Hereafter, we apply our

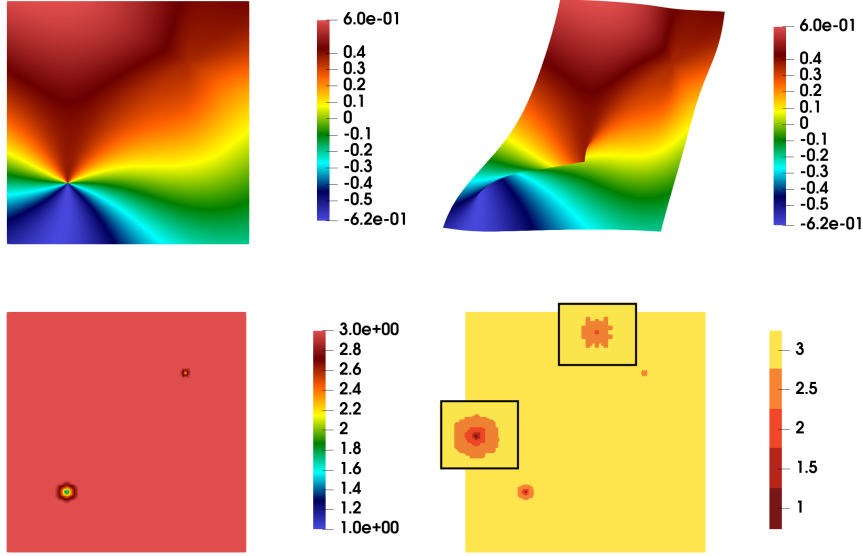


FIGURE 5. Top: Two-dimensional (left) and three-dimensional (right) plots of the function g defined in (17) on the unit square Ω . Bottom: Local Hölder exponents, displayed with linear (left) and structured (right) colormaps. We observe that g is in $C^{1-\frac{d}{2}}((0.25, 0.25)) = C^0((0.25, 0.25))$ and in $C^{2-\frac{d}{2}}((0.75, 0.75)) = C^1((0.75, 0.75))$.

method to the Shepp-Logan **Phantom**¹ to pinpoint the sharp boundaries between its homogeneous regions, which are clearly defined in the original picture. We convert the phantom to a 500×500 grayscale image (values ranging from 0 for black to 1 for white) and then apply our method to highlight its discontinuities. The result is displayed in Figure 6. As can be seen, all boundaries are correctly identified.

We also test our edge detector on noisy images, including MATLAB's **Visioteam**² dataset and a photograph of Lugano (Switzerland). Although the picture noise introduces many spurious high-frequency discontinuities, our method successfully highlights the true object boundaries. To visualize them, we threshold the local decay slopes, fitted with Algorithm 2, plotting only those regions where the estimated slope falls below 1.75, being able to capture the jumps plus some possible noise around the singularities. These experiments are performed at a resolution of 2048×2048 pixels. The resulting singularity detection is shown in Figures 7 and 8, respectively. As can be seen of the bottom rows of each of the figures, the boundaries are correctly identified after removing the noise.

5.4. Surface Detection. We show that the proposed method works also on manifolds with scattered data. We consider sample 4 million random points on the unit sphere \mathbb{S}^2 .

For a point $\mathbf{p} = (x, y, z) \in \mathbb{S}^2$ with spherical coordinates (θ, ϕ) where $\theta = \arctan(y/x)$ is the azimuthal angle and $\phi = \arccos(z)$ is the polar angle, we define the test function as:

$$(18) \quad f(\theta, \phi) = \mathcal{H}(g(\theta, \phi))$$

¹<https://it.mathworks.com/help/images/ref/phantom.html>

²<https://it.mathworks.com/help/vision/ref/vision.cascadeobjectdetector-system-object.html>

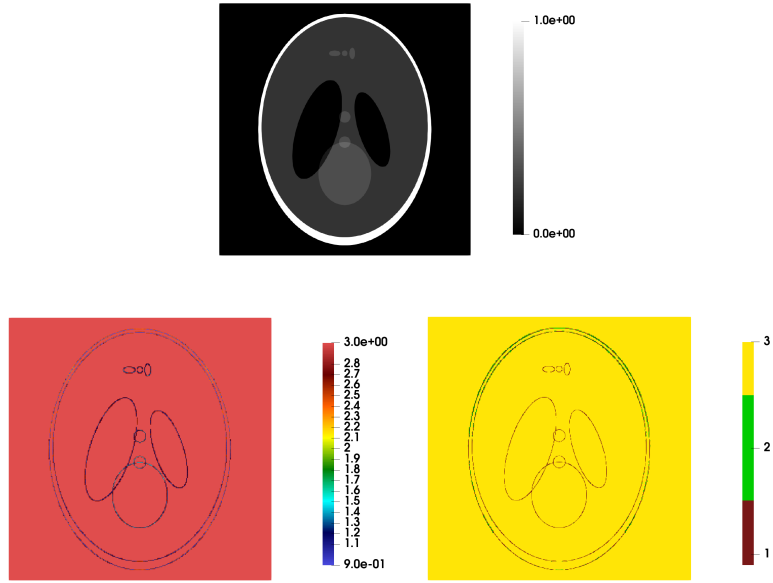


FIGURE 6. Top: Phantom function plot. Bottom: Local Hölder exponents, displayed with linear (left) and structured (right) colormaps. Our algorithm assigns the microlocal space $C^{1-\frac{d}{2}} = C^0$ to clusters intersecting the singularity.

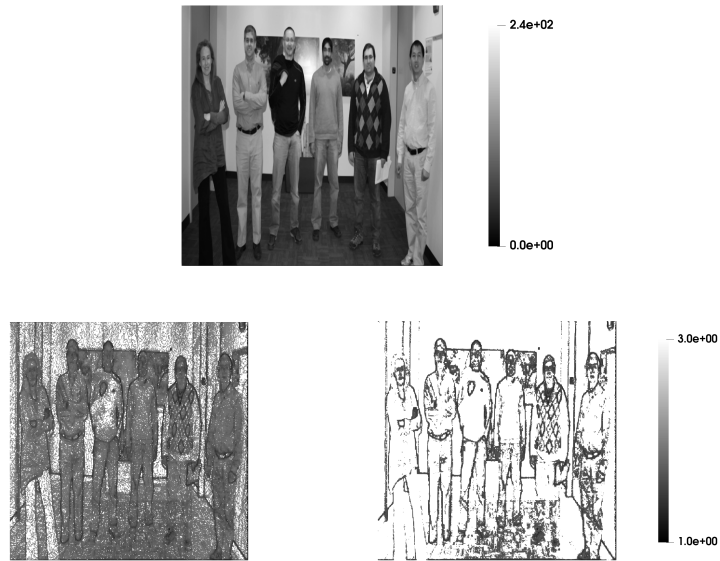


FIGURE 7. Top: Visionteam picture from Matlab. Bottom left: local Hölder exponents, where the image noise introduces spurious high-frequency exponents. Bottom right: thresholded coefficient map showing only values below 1.75, which reduces noise and better reveals the true boundaries.

where \mathcal{H} denotes the Heaviside step function and $g(\theta, \phi)$ is a composite pattern function given by:

$$(19) \quad g(\theta, \phi) = 0.5 \sin(3\theta) \sin(2\phi) + 0.3 \cos(2\theta) \cos(\phi) + 0.2 \sin(4\theta) \sin^2(\phi)$$

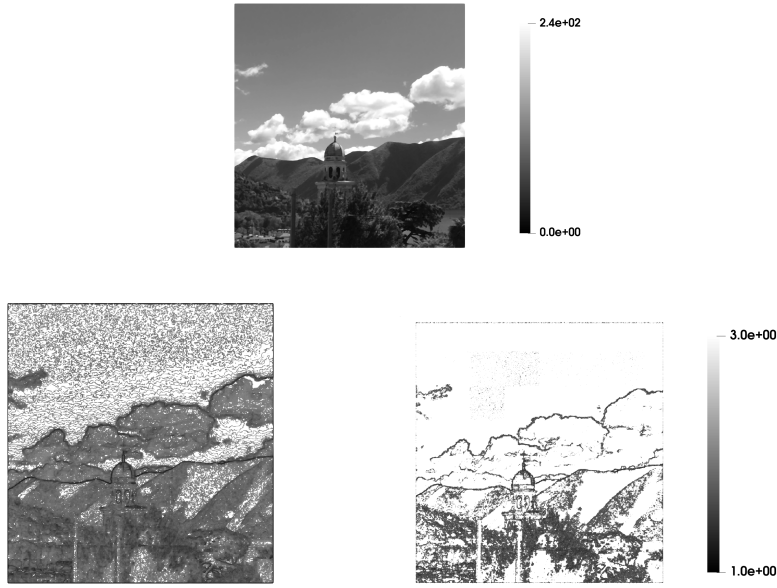


FIGURE 8. Top: photograph of the city of Lugano, Switzerland. Bottom left: local Hölder exponents, where the image noise introduces spurious high-frequency exponents. Bottom right: thresholded coefficient map showing only values below 1.75, which reduces noise and better reveals the true boundaries.

This construction creates a highly irregular boundary pattern that exhibits simultaneous rotational symmetries of different orders. The first term $\sin(3\theta) \sin(2\phi)$ generates a six-fold azimuthal symmetry with polar variation, while the second term $\cos(2\theta) \cos(\phi)$ contributes four-fold symmetry with emphasis towards the poles. The third component $\sin(4\theta) \sin^2(\phi)$ adds eight-fold azimuthal structure concentrated near the equatorial region. The results are shown in Figure 9. As can be seen, the local analysis over any small patch boundary

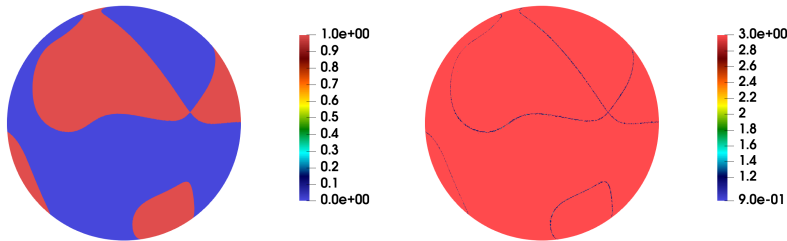


FIGURE 9. Left: Plots of the analyzed function on the unit sphere. Right: Local Hölder exponents. Our algorithm assigns the microlocal space $C^{1-\frac{d}{2}} = C^0$ to clusters intersecting the singularity.

yields the Hölder exponent of 0.

We also consider a more complex surface: the **Stanford Lucy** model from the Stanford 3D Scanning Repository³. We are provided with the mesh data for the Lucy surface and

³<https://graphics.stanford.edu/data/3Dscanrep/>

use only the vertex coordinates, which are approximately 1.4 million points, after removing non-manifold vertices to clean the dataset.

To construct a jump and a corner function, we embed the Lucy surface within a unit cube. We then introduce the singularities within the cube and project them onto the Lucy surface. Specifically, for visualization purposes, we create a jump along the cube's diagonal and a corner on the plane $x = 0.4$. The results are shown in Figure 10. The bottom row of



FIGURE 10. Top: Different angles of the Lucy domain with a jump and a corner function. Bottom: Local Hölder exponents. Our algorithm assigns the microlocal space $C^{1.5-\frac{d}{2}} = C^0$ to clusters intersecting the jump, and $C^{2.5-\frac{d}{2}} = C^1$ to clusters intersecting the corner.

the figure shows the obtained smoothness chart. As can be seen, all types of singularities are correctly identified.

5.5. Three-dimensional setting. We extend our analysis to a volumetric setting. We embed the **Stanford Bunny**, also from the Stanford 3D Scanning Repository⁴, into the unit cube. Using `libigl`⁵ to compute signed distance functions, we distinguish the points in the interior of the bunny from those of the exterior. For the points inside the bunny, we define a function f_{in} , and for the others, we define f_{out} , as follows

$$(20) \quad f_{\text{in}}(\mathbf{x}) = 10 \exp \left(\frac{-\|\mathbf{x} - \bar{\mathbf{x}}\|_2^2}{2\sigma^2} \right) \cdot \mathbb{1}_{\text{in}}(\mathbf{x}),$$

$$(21) \quad f_{\text{out}}(\mathbf{x}) = \|\mathbf{x} - \mathbf{x}_c\|_2 \cdot \mathbb{1}_{\text{out}}(\mathbf{x}),$$

where $\bar{\mathbf{x}}$ is the barycenter of the bunny, \mathbf{x}_c denotes the lower-left corner of the cube, and $\mathbb{1}_{\text{in}}(\mathbf{x})$ and $\mathbb{1}_{\text{out}}(\mathbf{x})$ are indicator functions. The result is illustrated in Figure 11. The bottom row of the figure shows the obtained smoothness chart. As can be seen, the boundary of the Stanford Bunny is correctly segmented and the right smoothness classes are attributed.

⁴<https://graphics.stanford.edu/data/3Dscanrep/>

⁵<https://github.com/libigl>

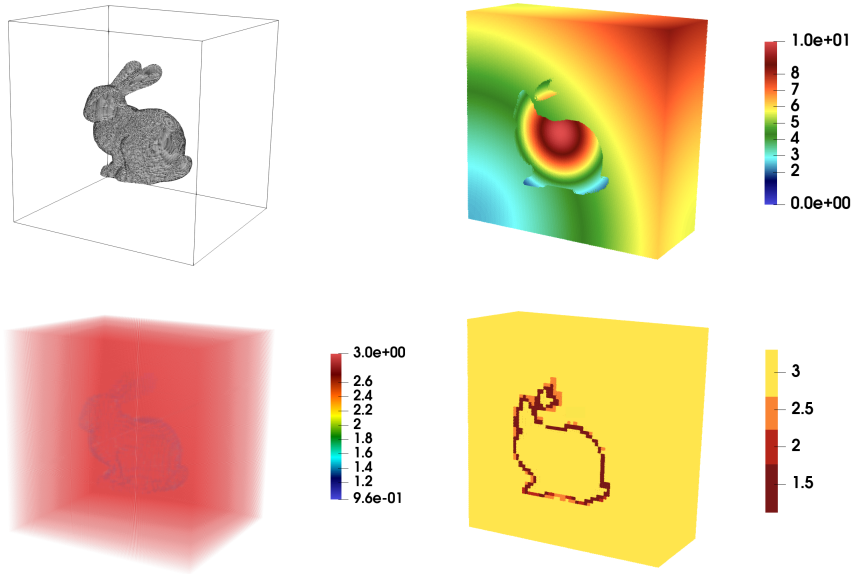


FIGURE 11. Top: Bunny embedded in the unit cube (left) and jump function (right). Bottom: Local Hölder exponents, displayed with linear (left) and structured (right) colormaps. Our algorithm assigns the microlocal space $C^{1.5-\frac{d}{2}} = C^0$ to those clusters intersecting the singularity.

5.6. Computational times. Finally, to give an idea of the entailed computational cost, we provide the run-times for all of the considered examples. The hierarchical clustering is performed using the top-down approach resulting in a computational cost of $\mathcal{O}(N \log N)$. Hence, we cannot expect an overall linear run-time. Even so, the results presented in table Table 1 show almost linear behavior, even when comparing across different dimensions and different data sites.

6. CONCLUSION

In the present paper we have addressed the problem of determining the local smoothness of non-uniformly sampled signals. To this end, we have employed samplets, which are a multiresolution analysis of localized discrete signed measures exhibiting vanishing moments. Taking the vanishing moment property and the localization as a starting point, we have derived decay estimates for the coefficients in the samplet expansions in terms of microlocal spaces. This approach allows to infer the local Hölder exponents of the signal and to discern different types of features, such as jumps and edges as well as smooth regions of the signal. Ultimately this allows to create a smoothness chart for the underlying signal, which directly gives a segmentation of the signal by thresholding. The construction of the samplet basis as well as the samplet transform can be performed in linear time in terms of the number of samples, once a multilevel hierarchy, typically a hierarchical cluster tree is provided. Depending if the latter is constructed bottom up or top down, the cost for the cluster tree is either linear or log-linear. As the creation of the smoothness chart can also be performed in linear time, we end up with an (essentially) linear cost approach for smoothness detection. The numerical results in one, two and three dimensions, ranging from non-uniformly sampled time series over images to point clouds, demonstrate the efficiency and the versatility of the approach.

Numerical setting	Number of data sites	Computational time (s)	
		Samplet tree	Slopes fitting
1D	1 000 000	0.98	0.03
Corner square	$2^{11} \times 2^{11}$	3.31	0.22
Singular points square	$2^{11} \times 2^{11}$	3.31	0.43
Shepp-Logan Phantom	1024×1024	0.83	0.05
Lugano	2048×2048	3.36	0.38
Visioteam	2048×2048	3.36	0.38
Jump cube	$2^8 \times 2^8 \times 2^8$	21.77	1.77
Corner cube	$2^8 \times 2^8 \times 2^8$	22.67	1.80
Sphere	4 000 000	6.86	0.48
Bunny	8 000 000	8.52	1.01
Lucy	1 400 000	2.05	0.16

TABLE 1. Computational times for samplet tree \mathcal{T} construction and slope fitting (using Algorithms 1 and 2) across the different numerical settings.

ACKNOWLEDGEMENT

The authors have been supported by the SNSF starting grant “Multiresolution methods for unstructured data” (TMSGI2 211684).

REFERENCES

- [1] S. Avesani, R. Kempf, M. Multerer, and H. Wendland. Multiscale scattered data analysis in samplet coordinates. *arXiv:2409.14791*, 2024. (to appear in SIAM J. Sci. Comput.).
- [2] P. Balazs and M. Multerer. Construction of generalized samplets in Banach spaces. *arXiv:2412.00954*, 2024.
- [3] D. Baroli, H. Harbrecht, and M. Multerer. Samplet basis pursuit: Multiresolution scattered data approximation with sparsity constraints. *IEEE Trans. Signal Process.*, 72:1813–1823, 2024.
- [4] G. Bertasius, J. Shi, and L. Torresani. Deepedge: A multi-scale bifurcated deep network for top-down contour detection. In *Proc. IEEE Conf. Comput. Vis. Pattern Recognit. (CVPR)*, pages 4380–4389, 2015.
- [5] S. De Marchi, W. Erb, F. Marchetti, E. Perracchione, and M. Rossini. Shape-driven interpolation with discontinuous kernels: Error analysis, edge extraction, and applications in magnetic particle imaging. *SIAM J. Sci. Comput.*, 42(2):B472–B491, 2020.
- [6] F. Demengel. *Functional Spaces for the Theory of Elliptic Partial Differential Equations*. Springer, London, UK, 2012.
- [7] S. Dorafshan, R. J. Thomas, and M. Maguire. Comparison of deep convolutional neural networks and edge detectors for image-based crack detection in concrete. *Constr. Build. Mater.*, 186:1031–1045, 2018.
- [8] O. Elharrouss, Y. Hmamouche, A. K. Idrissi, B. El Khamlichi, and A. El Fallah-Seghrouchni. Refined edge detection with cascaded and high-resolution convolutional network. *Pattern Recognit.*, 138:109361, 2023.
- [9] Y. Ganin and V. Lempitsky. N^4 -fields: Neural network nearest neighbor fields for image transforms. In *Asian Conf. Comput. Vis. (ACCV)*, pages 536–551. Springer, 2014.
- [10] A. Grossmann. Wavelet transforms and edge detection. In *Stoch. Process. Phys. Eng.*, pages 149–157. Springer, 1988.

- [11] H. Harbrecht and M. Multerer. Samplers: Construction and scattered data compression. *J. Comput. Phys.*, 471:111616, 2022.
- [12] H. Harbrecht, M. Multerer, O. Schenk, and Ch. Schwab. Multiresolution kernel matrix algebra. *Numer. Math.*, 156(3):1085–1114, 2024.
- [13] W. Huang, M. Valsecchi, and M. Multerer. Anisotropic multiresolution analyses for deepfake detection. *Pattern Recognit.*, 164:111551, 2025.
- [14] J.-J. Hwang and T.-L. Liu. Pixel-wise deep learning for contour detection. *arXiv:1504.01989*, 2015.
- [15] S. Jaffard. Pointwise smoothness, two-microlocalization and wavelet coefficients. *Publ. Mat.*, 35(1):155–168, 1991.
- [16] S. Jaffard and Y. Meyer. *Wavelet Methods for Pointwise Regularity and Local Oscillations of Functions*, volume 587. Amer. Math. Soc., Providence, 1996.
- [17] B. Jawerth and W. Sweldens. An overview of wavelet based multiresolution analyses. *SIAM Rev.*, 36(3):377–412, 1994.
- [18] J. Jing, S. Liu, G. Wang, W. Zhang, and C. Sun. Recent advances on image edge detection: A comprehensive review. *Neurocomputing*, 503:259–271, 2022.
- [19] J. H. Jung and V. R. Durante. An iterative adaptive multiquadric radial basis function method for the detection of local jump discontinuities. *Appl. Numer. Math.*, 59(7):1449–1466, 2009.
- [20] L. Lenarduzzi and R. Schaback. Kernel-based adaptive approximation of functions with discontinuities. *Appl. Math. Comput.*, 307:113–123, 2017.
- [21] J. Li. *A Wavelet Approach to Edge Detection*. PhD thesis, Sam Houston State Univ., M.Sc. Thesis, 2003.
- [22] S. Mallat. *A Wavelet Tour of Signal Processing*. Elsevier, San Diego, US, 1999.
- [23] S. Mallat and S. Zhong. Characterization of signals from multiscale edges. *IEEE Trans. Pattern Anal. Mach. Intell.*, 14(7):710–732, 1992.
- [24] P. Perona. Steerable-scalable kernels for edge detection and junction analysis. In *Proc. Eur. Conf. Comput. Vis. (ECCV)*, pages 3–18. Springer, 1992.
- [25] W. Shen, X. Wang, Y. Wang, X. Bai, and Z. Zhang. Deepcontour: A deep convolutional feature learned by positive-sharing loss for contour detection. In *Proc. IEEE Conf. Comput. Vis. Pattern Recognit. (CVPR)*, pages 3982–3991, 2015.
- [26] X. Soria, A. Sappa, P. Humanante, and A. Akbarinia. Dense extreme inception network for edge detection. *Pattern Recognit.*, 139:109461, 2023.
- [27] J. Sun, D. Gu, Y. Chen, and S. Zhang. A multiscale edge detection algorithm based on wavelet domain vector hidden markov tree model. *Pattern Recognit.*, 37(7):1315–1324, 2004.
- [28] R. Sun, T. Lei, Q. Chen, Z. Wang, X. Du, W. Zhao, and A. K. Nandi. Survey of image edge detection. *Front. Signal Process.*, 2:826967, 2022.
- [29] R. Tarjan. Depth-first search and linear graph algorithms. *SIAM J. Comput.*, 1(2):146–160, 1972.
- [30] V. Torre and T. A. Poggio. On edge detection. *IEEE Trans. Pattern Anal. Mach. Intell.*, 2:147–163, 1986.
- [31] R. Wang. Edge detection using convolutional neural network. In *Int. Symp. Neural Netw.*, pages 12–20. Springer, 2016.
- [32] S. Xie and Z. Tu. Holistically-nested edge detection. In *Proc. IEEE Int. Conf. Comput. Vis. (ICCV)*, pages 1395–1403, 2015.
- [33] L. Zhang and P. Bao. Edge detection by scale multiplication in wavelet domain. *Pattern Recognit. Lett.*, 23(14):1771–1784, 2002.
- [34] W. Zhang, Y. Zhao, T. P. Breckon, and L. Chen. Noise robust image edge detection based upon the automatic anisotropic gaussian kernels. *Pattern Recognit.*, 63:193–205, 2017.

SARA AVESANI, IDSIA USI-SUPSI, UNIVERSITÀ DELLA SVIZZERA ITALIANA, VIA LA SANTA 1, 6962 LUGANO, SWITZERLAND.

Email address: `sara.avesani@usi.ch`

GIANLUCA GIACCHI, IDSIA USI-SUPSI, UNIVERSITÀ DELLA SVIZZERA ITALIANA, VIA LA SANTA 1, 6962 LUGANO, SWITZERLAND.

Email address: `gianluca.giacchi@usi.ch`

MICHAEL MULTERER, IDSIA USI-SUPSI, UNIVERSITÀ DELLA SVIZZERA ITALIANA, VIA LA SANTA 1, 6962 LUGANO, SWITZERLAND.

Email address: `michael.multerer@usi.ch`